
Ground-Penetrating Radar for Close-in Mine Detection

Olga Lucia Lopera Tellez and Bart Scheers

Additional information is available at the end of the chapter

<http://dx.doi.org/10.5772/67007>

Abstract

In this chapter, two of the major challenges in the application of ground-penetrating radar in humanitarian demining operations are addressed: (i) development and testing of affordable and practical ground penetrating radar (GPR)-based systems, which can be used off-ground and (ii) development of robust signal processing techniques for landmines detection and identification. Different approaches developed at the Royal Military Academy in order to demonstrate the possibility of enhancing close-range landmine detection and identification using ground-penetrating radar under laboratory and outdoor conditions are summarized here. Data acquired using different affordable and practical GPR-based systems are used to validate a number of promising developments in signal processing techniques for target detection and identification. The proposed approaches have been validated with success in laboratory and outdoor conditions and for different scenarios, including antipersonnel, low-metal content landmines, improvised explosive devices and real mine-affected soils.

Keywords: ground-penetrating radar, clutter reduction, object detection, landmines

1. Introduction

To make reliable, easily interpreted and less time-consuming operational systems for landmine detection is a real challenge [1, 2]. Nowadays, demining is performed by using different kinds of demining systems, e.g., mechanical excavation, trained dogs/rodents, and metal detectors (**Figure 1**). Metal detector (MD) is one of the most used close-range detection systems for demining. However, antipersonnel (AP) landmines are not made any more with significant amounts of metal but with plastic and other nonmetallic elements. Metal detection-based systems available today do not efficiently detect plastic landmines with minimum metal content in a metal debris contaminated area. In order to compensate for small metal content



Figure 1. An example of classical demining operations in Croatia: deminers scan with metal detectors and trained dogs after the mechanical excavation [4].

in modern landmines, some sensors offer the possibility to the operator to increase their sensibility. However, the number of false alarms rises. Cambodian deminers are confronted with this problem daily. For each detected AP landmine, more than 500 inoffensive metallic debris such as grenade fragments and cartridges are located (some results collected after visiting a Cambodian mine-field, **Figure 2**). False alarm rate as well as misdetection of low and nonmetal content of AP landmines have made mine clearance operations dangerous, time consuming, and expensive.

During the 1990s, several research groups started contributing in solving this problem by developing hardware and software for demining applications [1–3]. However, only a few are currently employed in real mine-affected areas. One of these relatively new technologies is ground penetrating radar (GPR), an attractive choice for landmine detection due to their advantages over other sensors. GPR can detect both metallic and plastic mines in a variety of



Figure 2. Some of the objects found after demining operations with metal detectors in the M7753 minefield, Province of Siem Reap, Cambodia [4].

soils by noninvasive subsurface sensing [3]. GPR sends a series of microwave pulses ranging from about 1 to 4 GHz into the ground. It then looks for anomalies in the reflected signal, which could indicate the presence of a landmine. In terms of buried target detection, the strength of radar echoes is usually associated with contrasts of electromagnetic characteristics between targets and their surrounding soils. For antipersonnel mines, GPR is usually used in combination with a metal detector [3, 4]. The metal detector would detect all metal contents in the soil, and the GPR is used to discriminate on the size of the objects: smaller metal objects are discarded and larger metal objects are confirmed as dangerous. Note that the GPR has the capacity to detect nonmetal mines. But when used alone its possible large false alarm rate makes it more suited to look for antitank mines. Moreover, its weight can be light, so that it can be installed in a hand-held system or in a vehicle-mounted system in the form of an array of multiple antenna elements [3].

This chapter addresses two of the major challenges in the application of GPR in humanitarian demining operations: (i) development of affordable and practical GPR-based systems and (ii) development of robust GPR signal processing techniques for landmine detection and identification. This chapter also reviews research carried out at the Royal Military Academy in these topics.

2. GPR systems

2.1. GPR principles

Electrical properties of materials are determined by electrical conductivity, permittivity and permeability, which are function of frequency. The relative permittivity (or dielectric constant) of a medium impacts the electric field propagation and is the most important parameter for GPR. The relative permeability affects the magnetic field propagation. The electromagnetic wave attenuation in the subsurface is strongly dependent on the electrical conductivity of the medium and its variation. The latter is normally controlled by water [4–8]. For a conductive material, the electromagnetic field is diffusive and cannot propagate as an electromagnetic wave. When it is resistive, or dielectric, an electromagnetic field can propagate as an electromagnetic wave. When an electromagnetic wave is sent into the ground, GPR measures the reflected echoes from any electrical property discontinuity in the subsurface structure. **Figure 3** shows a block diagram of a generic GPR system [5].

The velocity and reflectivity of the electromagnetic wave in soil are characterized by the dielectric constant (relative permittivity) of the soil. When the dielectric constant of the soil is ϵ_r , the propagation velocity of electromagnetic waves in this medium is given by

$$v = \frac{c}{\sqrt{\epsilon_r}} \quad (1)$$

where $c = 3 \times 10^8$ m/s. Note then that in air ($\epsilon_r = 1$), the propagation velocity is then $v = c$. Dielectric constants measured at 100 MHz for different materials [3] are listed in **Table 1**.

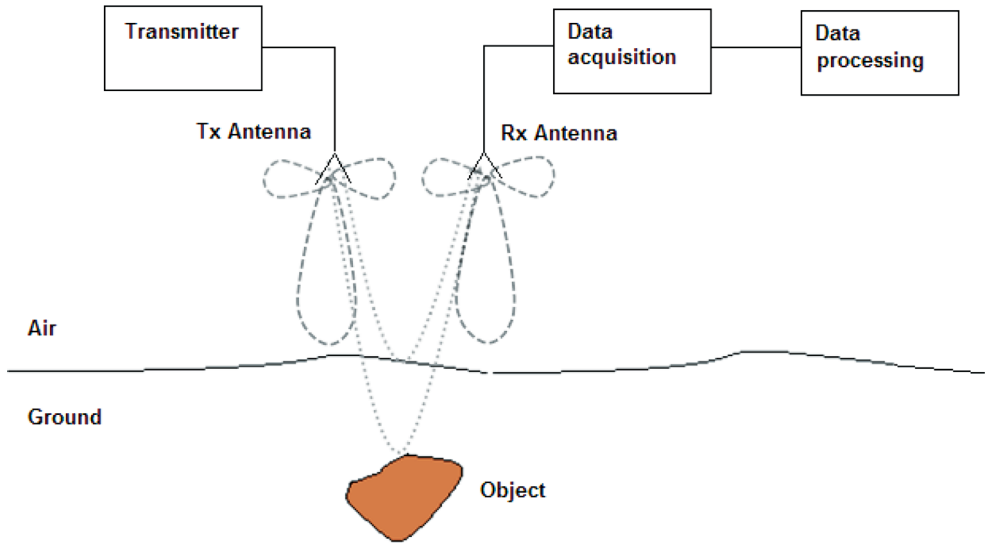


Figure 3. Block diagram of a generic GPR system [5].

Material	Attenuation (dB/m)	Relative permittivity ϵ_r
Air	0	1
Clay	10–100	2–40
Concrete: dry	2–12	4–10
Concrete: wet	10–25	10–20
Fresh water	0.1	80
Sand: dry	0.01–1	4–6
Sand: saturated	0.03–0.3	10–30
Sandstone: dry	2–10	2–3
Sandstone: wet	10–20	5–10
Seawater	1000	81
Soil: firm	0.1–2	8–12
Soil: sandy dry	0.1–2	4–6
Soil: sandy wet	1–5	15–30
Soil: loamy dry	0.5–3	4–6
Soil: loamy wet	1–6	10–20
Soil: clayey dry	0.3–3	4–6
Soil: clayey wet	5–30	10–15
TNT	–	3
Plastic	–	2–4

Table 1. Attenuation and relative permittivity of subsurface materials measured at 100 MHz [3].

When GPR transmits electromagnetic waves from a transmitting antenna located off-the-ground, signals travel in the air layer and when the electromagnetic wave encounters any dielectrical discontinuity, a reflection occurs. The latter is received by a receiving antenna, located off-the-ground, and it is referred to as an A-scan, e.g., a single waveform recorded by GPR, with the antennas at a given position (x, y) . In this data set, the time t is the only variable, related to the depth z by the propagation velocity of the EM waves in the medium. Its representation in the time domain can be seen in **Figure 4** [5]. The time axis or the related depth axis is usually pointed downward.

When moving the GPR antennas on a line along the x -axis, a set of A-scans can be gathered, which form a two-dimensional (2D) data set called a B-scan (**Figure 5**). When the amplitude of

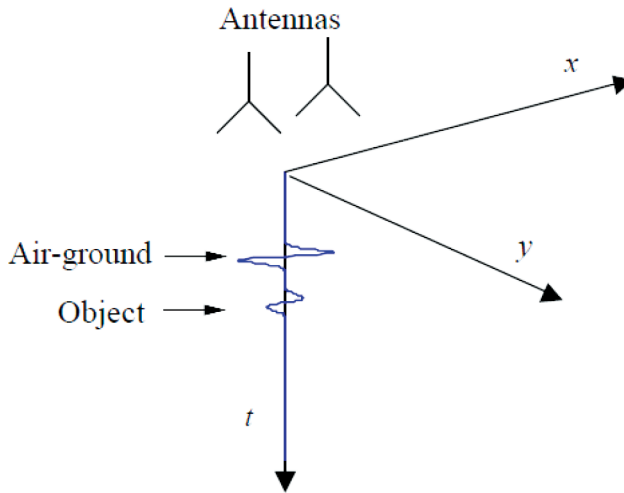


Figure 4. Representation of an A-scan [5].

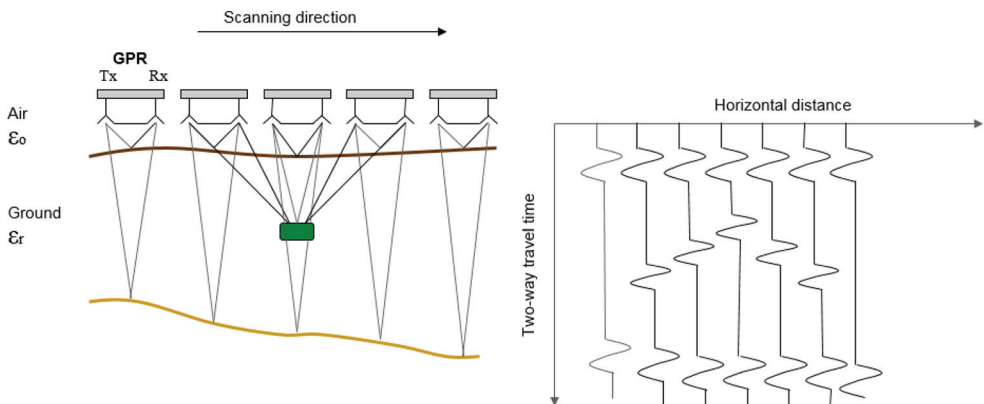


Figure 5. Configuration and representation of a B-scan.

the received signal is represented by a color scale (e.g., gray-scale), a 2D image is obtained and is shown in **Figure 6**. The 2D image represents a vertical slice in the ground. Reflections on a point scatter located below the surface appear, due to the beamwidth of the transmitting and the receiving antenna, as hyperbolic structures in a B-scan. Finally, when moving the antenna over a (regular) grid in the xy -plane, a three-dimensional (3D) data set can be recorded, called a C-scan (**Figure 6**). Usually a C-scan is represented as a two-dimensional image by plotting the amplitudes of the recorded data at a given time t_i . The resulting image represents then a horizontal slice at a certain depth, parallel to the recording plane (**Figure 7**). Nowadays, many user-software packages (e.g., GPRMax2D and 3D [7]) have integrated functions to plot directly two- or three-dimensional representations of the recorded C-scans. Examples of these plots are: (i) an arbitrary cut in the 3D volume and (ii) an isosurface (surface with the same amplitude), both represented in **Figure 7** [5].

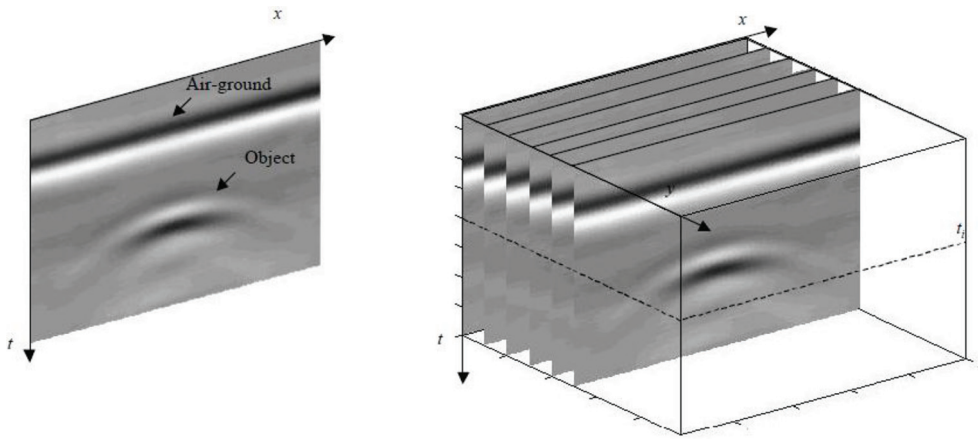


Figure 6. A gray-scale illustration of a B-scan (left) and a series of B-scans forming a C-scan (right).

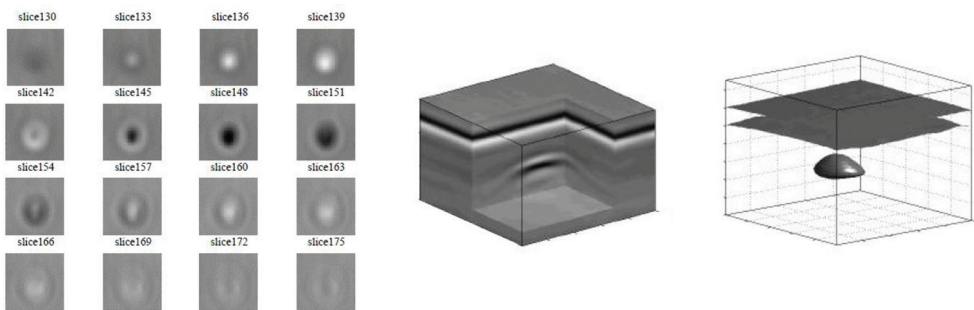


Figure 7. Representation of a C-scan by horizontal slices at different depths (left), arbitrary cut in the 3D volume (center), and isosurface (right) [5].

2.2. GPR design

Table 2 gives a schematic overview of the various possible types of GPR systems that exist today. GPR systems can be classified by the domain in which they work and by the type of modulation. GPR systems operate either in time domain or in frequency domain. In the time domain GPR there are two major categories: the amplitude modulated and the carrier-free GPR. The first one sends a pulse with a carrier frequency. This carrier frequency is modulated by a (square) envelope. Good depth resolution is achieved by reducing the duration of the pulse as short as possible. Most of the commercially available GPRs belong to this group [5].

The need for larger bandwidth has led to the development of a second category of time domain GPR: the carrier-free GPR. The pulse sent by the GPR has no carrier. The shape of the pulse can vary, but typically a Gaussian pulse is used. The carrier-free radar is also called an ultra-wide band (UWB) GPR because of the large bandwidth. Before, GPR systems were developed based on time domain waveform. Nowadays GPRs are also developed in the frequency domain. In the latter, systems can have two possible modulation types: either the frequency modulated (FM) continuous wave (CW) or stepped frequency (SF) GPR [5].

FM systems transmit a carrier frequency, which changes continuously by using a voltage-controlled oscillator over a certain frequency range. The frequency sweeps according to a function within a certain time. After reception, the reflected wave is mixed with the emitted one, and the target depth can be calculated from the difference in frequency between the transmitted and received wave. FM systems have poor dynamic range, which is an important limitation. Since FM radars receive signals at the same time as it is transmitting, leakage signals between the antennas can obscure small reflections. Those two facts deviate the attention from FM systems to SF radars for ground applications.

An SF GPR uses a frequency synthesizer to go through a range of frequencies equally spaced by an interval Δ . At each step, a CW is send with a high stability and mixed with the received signal using a quadrature mixer. For each frequency, the amplitude and phase of the received signal are compared with the transmitted signal [5]. The reader can refer to Ref. [9] for a good overview of this technique. Stepped-frequency continuous-wave (SFCW) radars have some advantages over the others, including wider dynamic range and better signal-to-noise ratio (SNR) [3, 5, 6].

Besides the domain of operation, GPR antennas may be either monostatic (single emitting and receiving antenna), bistatic (different emitting and receiving antenna), or an array configuration of different antenna types and sizes. In the mine detection application, high depth resolution is needed and therefore ultra-wide band (UWB) antennas play an important role [8].

GPR design options				
Domain	Time		Frequency	
Modulation	Amplitude (mono cycle)	Carrier-free	Linear sweep	Stepped frequency

Table 2. Different types of GPR systems.

Vehicle-based systems generally use array antenna mode [10] in combination with other sensors such as metal detectors [11]. Laboratory prototypes of UWB GPR systems are built in bistatic mode [12, 13], and such a configuration is adopted for hand-held GPR-based systems [14, 15]. For all these configurations, different types of antennas such as horn, loop, spiral, Vivaldi, and combinations of them are used. An overview of their characteristics, advantages, and drawbacks for demining applications can be found in Refs. [5, 16].

2.3. UWB GPR laboratory prototypes

Landmine detection using GPR is a very particular problem. Commercial GPRs are mostly designed for geophysical applications and use central frequencies up to 1 GHz. As landmines are small objects, a large bandwidth is needed for a better depth resolution. Therefore, we have decided to build our own UWB system in the frame of the HUDEM (Humanitarian Demining) project (in collaboration with the Microwave Engineering and Applied Electromagnetism Department of the Catholic University of Louvain, UCL) and to use a GPR-based system (under the BEMAT (Belgian Mine Action Technologies) project) developed at the Environmental Sciences Institute of the UCL. These choices were made following five technical and practical requirements [5]:

1. The GPR system must be UWB (working in the frequency range 500 MHz to 4.5 GHz).
2. The GPR system must be used off ground (safety reasons and to increase mobility of the system, see point 3 below). Therefore, the antenna must be highly directive in order to couple sufficient energy into the ground for achieving a penetration depth of 15 cm in any soil [17].
3. The GPR system must guarantee a high degree of mobility, i.e., attention should be paid to dimensions and weight. Minefields have often rough surfaces, steep slopes and/or are covered with dense vegetation. Not all systems can guarantee a sufficient flexibility in such scenes.
4. The antenna properties must be independent of the ground properties.
5. The GPR system must be cheap in production to limit the overall cost of the sensor. This will always be asked for in the case of humanitarian demining.

2.3.1. Development of a transverse electromagnetic horn antenna

Based on the requirements listed before, many researchers have focused their attention into transverse electromagnetic (TEM) horn antennas, which have a high directivity, can work broadband and are nondispersive. A traveling wave TEM horn consists of a pair of triangular conductors forming a V structure (**Figure 8**), which can transmit and receive a fast transient pulse [18, 19]. It is presumed that the TEM horn conducts mainly the TEM mode within a selected frequency range by conserving constant characteristic impedance and that, by omitting the edge diffraction effect and fringe fields, a linearly polarized spherical wave is diffused.

This type of antenna is totally parameterized by three characteristics: L is the length of the antenna plates, φ_0 is the azimuth half-angle, and θ_0 is the elevation half-angle. The characteristic impedance of an infinite long TEM horn ($L = \infty$) only depends on the two angles φ_0 and

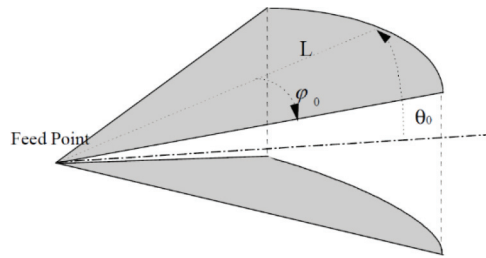


Figure 8. Conventional design of the TEM horn antenna characterized by three parameters: L the length of the antenna plates, φ_0 the azimuth half-angle, and θ_0 the elevation half-angle.

θ_0 . In theory, a TEM mode does not have an upper cut-off frequency; however, this upper cut-off frequency will be practically restricted. The length L mainly determines the lower cut-off frequency.

For improving the directivity and reducing the physical antenna dimensions without diminishing the bandwidth, TEM horns can be filled with a silicone. A silicone characterized by a real relative permittivity ϵ_r of 2.89 and a loss tangent of 0.0084 at 1 GHz is used. As a result, the propagation speed of the TEM wave between the antenna plates will be divided by $\sqrt{\epsilon_r}$ (or the electrical length of the antenna will be increased by a factor $\sqrt{\epsilon_r}$) and the surge impedance will be reduced by a factor $\sqrt{\epsilon_r}$ [20].

For preserving the same surge impedance as without the silicone, the angle θ_0 can be increased, which improves the directivity. In this case, the antenna impedance is chosen to match the 50Ω driving cable. As a result, no mismatches will be found at the part of the transient traveling current that bounces back at the antenna aperture toward the excitation source, avoiding antenna ringing. The principle seems to work well for frequencies in the band of the antenna [20].

The antenna plates are replaced by printing sets of 41 wires on circuit boards (**Figure 9**). Since the distance between the wires is small, the antenna characteristics are preserved. In addition,

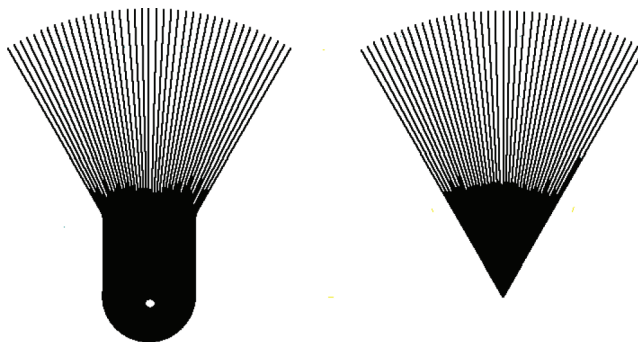


Figure 9. Lower and upper antenna plates, etched on a printed circuit board.

the currents are forced to be radial, limiting the surface of conducting metal. In this application, this is of great importance since GPRs are often used in combination with metal detectors.

In order to feed the TEM horn in its balanced configuration (**Figure 8**) with an unbalanced coaxial line, an UWB (frequency-independent) balun is required to prevent currents on the coax. Several realizations of a TEM horn were made, and, at first, measurements revealed an unbalanced current component on the coax exterior. This means that the coaxial feedline was reacting as an antenna. A common way of eliminating such currents is to add chokes (ferrite cylinders) around the feeding cable [21]. For this design, a new kind of balun is tested, which principle lays on an electrostatic reasoning described in Ref. [22]. The function of the taper in the bottom plate is to provide a gradual transition between the unbalanced upper antenna plates on a ground-plane, toward a balanced alignment with two symmetrical antenna plates. However, a slide change of the surge impedance along the antenna is introduced by such a transition. The surge impedance of one antenna plate on a ground-plane is half the value calculated using the wire model. Since θ_0 in the unbalanced configuration is measured from the ground plane, the resulting value will double the elevation half-angle of the balanced configuration. As a result, the surge impedance of the unbalanced part is found to be slightly inferior to the surge impedance of the balanced part of the antenna. Using the wire model and taking into account the reduction of the surge impedance due to the filling and the influence of the balun, an elevation half-angle θ_0 (defined in the balanced part) of 14.5° is calculated to match 50Ω . Summarizing, the antenna parameters are $L = 12 \text{ cm}$, $\varphi_0 = 30^\circ$, and $\theta_0 = 14.5^\circ$, which leads to a physical antenna aperture of $12 \text{ cm} \times 6 \text{ cm}$.

The dielectric-filled antennas were integrated in a laboratory UWB GPR. For this, a study was made in order to optimize the position and orientation of the Tx and Rx antennas. To reduce the coupling between the two TEM horns, they were put side by side with a common H-plane (E-field of both antennas is parallel to the interface). Generally speaking, antenna coupling is not critical since it could be neutralized. However, if the ringing between the two antennas lasts too long, it could obscure interesting parts of the returned signal. After some tests, the antennas were fixed at around 25 cm above the surface [12].

When configuring the Tx-Rx antenna system, it is important to consider the two antennas as one antenna. Therefore, the combined antenna pattern should be analyzed. The 3 dB beamwidth that results of this combination is normally function of the offset angle θ_1 , as shown in **Figure 10**. When moving the GPR antennas over a fix target, in the backscattered signal displayed as function of time (B-scan) a hyperbolic structure will appear (**Figure 6**). A wider 3 dB beamwidth will produce wider hyperbolas in the B-scan and could therefore improve the detection of objects. The total energy found in these hyperbolic structures is considered as a measure for the optimization of the offset angle θ_1 . The expected reflected energy of the object is represented by this total energy, after focusing the B-scan using an optimal migration methodology. In order to optimize the offset angle, different synthetic B-scans of a buried object at 6 cm depth are simulated for different values of θ_1 [12]. An offset angle of 20° is found to produce the hyperbola with the maximum of energy. In the configuration consider for this calculation (object at a depth of 6 cm), 20° corresponds to the angle that focuses the antennas on the object, considering the refraction. In a real scenario, the object is buried at an unknown depth, which is expected to be

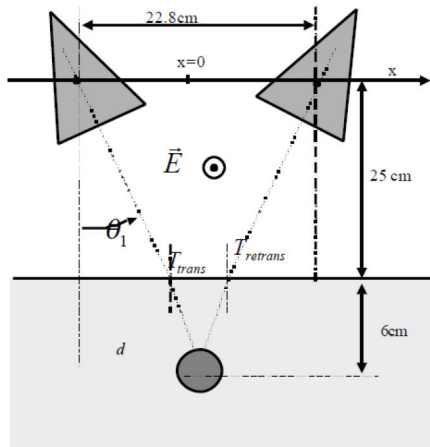


Figure 10. Dielectric-filled TEM horn antenna configuration in bistatic mode [12].

no deeper than 20 cm. Therefore, when building the laboratory UWB GPR, an angle θ_1 of 20° was selected.

Figure 11 represents a GPR image of a PMN AP landmine (12.5 cm diameter, plastic case), buried at 1 cm depth in dry sand. Data are acquired by an impulse UWB GPR emulated using a picosecond pulse labs step-generator type PSPL 4050B, followed by an impulse-forming-network and connected to two identical dielectric-filled TEM horn antennas. Data are taken by displacing the Tx and Rx antennas by steps of 1 cm (represented on the x -axis). In each antenna position, a short Gaussian impulse is radiated and the backscattered signal is recorded (y -axis).

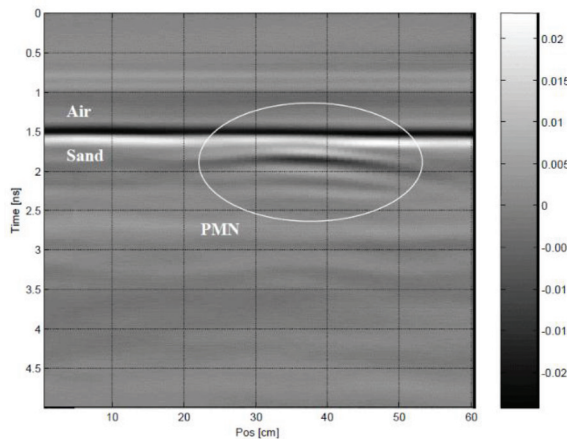


Figure 11. Time domain representation of the impulse UWB GPR measurements performed on sand for the PMN AP mine, buried at 1 cm.

2.3.2. UWB SFCW GPR in monostatic mode

An SFCW system is considered in the frame of the BEMAT project, which also covers several of the requirements mentioned before. It is based on the frequency domain radar-antenna-multi-layered medium model developed by Lambot et al. [23], which applies for SFCW radars operating off the ground in monostatic mode (in our case, a portable vector network analyzer (VNA) connected to a monostatic horn antenna, see **Figure 12**). In this approach, it is assumed that the distribution of the backscattered electric field measured by the antenna does not rely upon the elements of propagation (air and subsurface layers), i.e., only the amplitude and phase of the field change. Therefore, the antenna can be described by a model of linear transfer functions in series and in parallel, acting as global transmittances and reflectances (**Figure 13**).

In this model, $G(\omega)$ is the soil response and $H_i(\omega)$, $H_t(\omega)$, $H_r(\omega)$, $H_f(\omega)$ are, respectively, the antenna return loss, the antenna transmitting and receiving transfer functions, and the antenna feedback loss, which have to be determined, with ω being the angular frequency. The antenna equation can be written as

$$S(\omega) = H_i(\omega) + \frac{H_t(\omega)H_r(\omega)G(\omega)}{1 - H_f(\omega)G(\omega)} \quad (2)$$

The latter equation is represented in the frequency domain and the transfer functions are frequency dependent complex quantities. The multiple wave reflections occurring inside the antenna, which, as stated before, are a result of the impedance differences between the antenna feed point and the antenna aperture are represented by the return loss function $H_i(\omega)$. Such inner wave reflections are independent of the medium, $H_t(\omega)$ and $H_r(\omega)$ constitute the antenna gain and phase delay between the VNA calibration plane (the connection between the antenna



Figure 12. The UWB SFCW GPR system emulated using the hand-held VNA connected to the horn antenna via a 50-Ohm N-type coaxial cable.

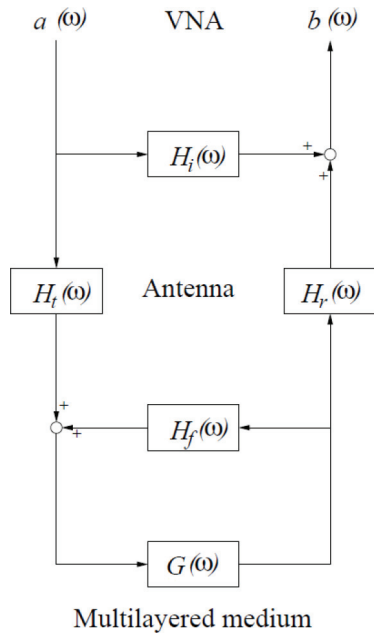


Figure 13. The VNA-antenna-multilayered medium system modeled as linear transfer functions in series and in parallel.

feed point and the VNA cable) and the source and receiver virtual point (antenna phase center). The feedback loss transfer function $H_f(\omega)$ represents multiple wave reflections between the antenna and the subsurface. $H_i(\omega)$ and $H_f(\omega)$ are global reflectances, and $H_t(\omega)$ and $H_r(\omega)$ are global transmittances. Finally, $G(\omega)$ accounts for the air-soil system [23] and is defined by a Green's function, solution of the 3D Maxwell's equations for electromagnetic waves propagating in horizontally multilayered media [24].

The antenna transfer function $H_i(\omega)$ can be determined from using a measurement in free space conditions, for which $G(\omega) = 0$. Therefore, from Eq. (2) $H_i(\omega) = S_{fe}(\omega)$. The antenna transfer functions $H_t(\omega)$, $H_r(\omega)$, and $H_f(\omega)$ are determined using measurements at two different heights above a planar metal sheet (considered as an infinite perfect electric conductor), for which $G(\omega)$ is known accurately, and correspond therefore to a specific distribution of the measured electromagnetic field. Consider $H(\omega) = H_t(\omega) H_r(\omega)$, then

$$H_f(\omega) = \frac{\frac{S^b(\omega)}{G^b(\omega)} - \frac{S^a(\omega)}{G^a(\omega)}}{S^b - S^a} \tag{3}$$

$$H(\omega) = \frac{S^a(\omega)}{G^a(\omega)} - S^a(\omega)H_f(\omega) \tag{4}$$

On the one hand, a necessary condition for this antenna model is to employ the antenna sufficiently far from the surface. On the other hand, it is necessary to minimize losses by spherical

divergence in wave propagation, keep a high SNR, and ensure a high spatial resolution, conditions that are achieved by minimizing the distance between the antenna and the surface. In Ref. [25], laboratory experiments were carried out to characterize the transfer functions $H_i(\omega)$, $H(\omega)$, and $H_f(\omega)$ of a horn antenna (the antenna used in this study) as a function of height to determine to which extent they are still correct when approaching the soil surface. For this, electromagnetic measurements were carried out with the antenna aperture situated at 30 different heights h (from 1 to 28 cm) above a metal sheet of $2 \times 2 \text{ m}^2$. Results shown small errors on the calculation of the transfer functions for $h > 12 \text{ cm}$. Below $h \cong 12 \text{ cm}$, these errors appear to increase, resulting in important errors in the calculation of the soil response $G(\omega)$ for field applications. These results indicate that, in the application of landmine detection, the independency of the received field distribution with respect to the medium is maintained when the antenna aperture is at minimum $h = 12 \text{ cm}$.

In order to emulate the UWB SFCW radar, a low-cost hand-held VNA connected to a monostatic horn antenna via a 50 N-type coaxial cable is used. The VNA comprises a spectral analyzer (FSH6, Rohde and Schwarz), which uses a bridge and power divider (VSWR, Rohde and Schwarz) to give vector measurements. A linear polarized double-ridged broadband horn antenna (BBHA 9120A, Schwarzbeck Mess-Elektronik), with 22 cm length and $14 \times 24 \text{ cm}^2$ aperture area, is used to collect data. For this application and from antenna characteristics, it can be considered as directive (3-dB beamwidth of 45° in the E-plane and 30° in the H-plane at 1 GHz and 27° in the E-plane and 22° in the H-plane at 2 GHz, when working in the 0.8–5.0 GHz frequency range).

This UWB SPCW radar is easy to use and affordable, and it covers several of the requirements listed before. It has a linear dynamic range of 60 dB, allowing detecting weak scatterers. Internal reflections inside the antenna are accurately calculated and included in the EM model described before. As a result, they do not influence negatively the signal-to-noise ratio of the system. Besides, amplitude drift (that can be due to mechanical or temperature changes on the connection point of the antenna) is limited by a precise and easy-to-do calibration method using a standard Open-Short-Match calibration kit. While gathering data, this calibration could be performed once more.

Figure 14 shows a time domain representation of radar measurements performed in a homogeneous sand for the PMN AP landmine (12.5 cm diameter, plastic case) buried at 10 cm. The horn antenna was displaced over the x -axis following constant steps of 2 cm. The height of the antenna aperture is 20 cm above the soil surface.

2.4. Hand-held dual-sensors

During the past 10 years, the development of GPR applied to landmine detection has evolved from the laboratory conditions and test fields to real minefields. Nowadays, systems using dual sensor technology combining MD and GPR (hand-held dual sensors) have enabled improved discrimination against small metal fragments to be demonstrated in live minefields. Some of them have reached the stage where they are being produced in large numbers. Such

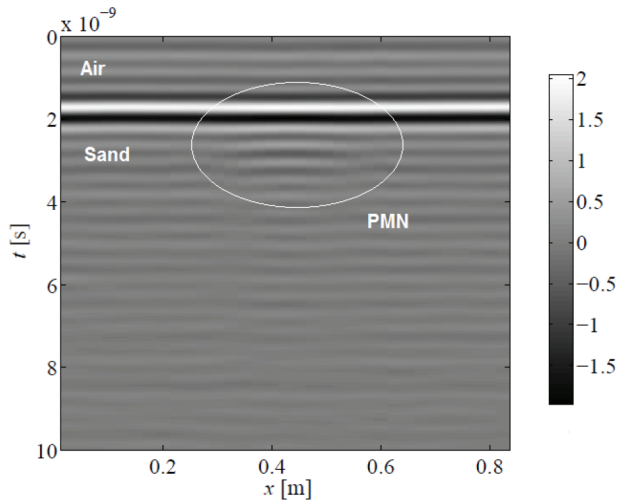


Figure 14. Time domain representation of the SFCW UWB GPR measurements performed on sand for the PMN AP mine, buried at 10 cm.

systems work with both MD and GPR, and they differ on the operating principle of GPR, the signal processing and the user interface. In this section, three of them are introduced.

MINEHOUND/VMR2 has been developed by ERA Tech., U.K., in collaboration with Vallon GmbH, Germany. It combines a pulse induction MD and an impulse GPR. This dual-sensor transforms MD and GPR signals into two separated audio signals of different frequency of vibration and tone. MINEHOUND/VMR2 has been tested in different mine-affected countries including Afghanistan, Angola, Bosnia and Cambodia [26].

ALIS (Advanced Landmine Imaging System) is a Japanese detector developed at the Tohoku University. It incorporates an MD and a GPR, in combination with a sensor tracking system, which makes possible to analyze and visualize the data (after migration). Its hand-held version is equipped with a VNA-based GPR and a pulse induction MD. This dual-sensor provides two different user interfaces: audio for MD signal and images for both MD and GPR signals. Different trials have been performed with ALIS in mine-affected countries including Afghanistan, Cambodia, Croatia, and Egypt [27].

AN/PSS-14 (former HSTAMIDS, Hand-held Standoff Mine Detection System) was originally a project founded by the Defense Advanced Research Projects Agency, DARPA, U.S., and has been produced later by CyTerra Corp. (now L3 Communications). It is equipped with a pulse induction MD and a GPR based on a wide-band, SF radar. AN/PSS14 gives to the user an audio signal when a metallic object is detected. If there is a metal detection and the GPR system identifies other mine-like material as well, a second sound, of a different frequency of vibration and tonality, is played as aided target recognition. This system has been produced since 2006 for U.S. Army operations in Iraq [28].

3. GPR signal processing

GPR principal function is to detect differences on the electromagnetic (EM) properties in the soil-target medium. This permits to locate even low and nonmetallic landmines. Apart from the response from a potential target, the backscattered signal carries also undesirable effects from antenna coupling, system ringing and subsurface reflections, which hide the target signature [1–3]. These effects have to be filtered out from the signal to enhance landmine detection.

3.1. Clutter

As stated before, using GPR in landmine detection operations could be advantageous since the number of false alarms could be reduced and since low-metallic content landmines that are not detected by metal detection could be detected by GPR. However, extracting the landmine signature from GPR data is negatively affected by a list of influencing elements categorized as clutter, which can partly or totally obscure or deform the backscattered signal from a buried object. Mainly, these influencing elements are: (1) antenna reactions causing multiple reflections and signal deformation; (2) the subsoil EM characteristics and their spatiotemporal distribution controlling wave propagation velocity, attenuation, and surface and subsoil reflections; (3) the EM variation between the buried object and the subsoil influencing the strength of the landmine response; and (4) surface roughness causing diffuse scattering. Thus, it is necessary to investigate suitable techniques in order to reduce clutter while maintaining high landmine detection rates. This could be very challenging due to the complicated EM phenomena taking place in the theoretically unknown antenna-air-soil-mine system.

Different approaches are used to reduce this clutter and to recognize the landmine signal. Widely used approaches to reduce clutter are average and moving average background subtraction (BS). Other BS techniques are based on wavelet transform and system identification. Once these approaches suppress part of the clutter, the next expected procedure is to detect the buried object. In this step, different signal processing techniques for the identification of the target signal are applied, including advanced algorithms for hyperbola detection [29], convolutional models and migration techniques [5]. An overview of different signal processing techniques for landmine detection using GPR can be found in Refs. [1, 3].

3.2. Filtering antenna effects and soil surface reflection

In Ref. [30], we propose a method to filter out the antenna internal reflections and multiple reflections between the antenna and the ground, as well as the related distortion effects, by using the frequency-dependent linear transfer functions model developed in [23]. These functions also account for the antenna gain and wave propagation time, fixing time-zero at the antenna phase center. An example of data before and after filtering the antenna effects is presented in **Figure 15** (note that in the radar data represented in **Figure 14**, these effects were previously removed).

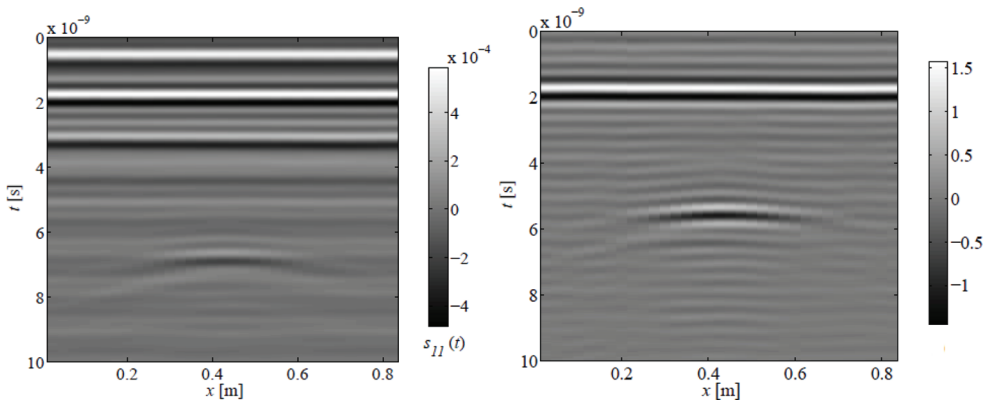


Figure 15. Time domain representation of the SFCW UWB GPR measurements performed on sand for an antitank (AT) mine, buried at 30 cm depth, before (left) and after (right) removing antenna effects.

On the left image we can observe the multiple reflections occurring in the antenna, between about 0 and 2 ns. These unwanted signals obscure the backscattered response when looking down in the time axis. At around 3.2 ns, the air-soil interface reflection appears. Then, a second-order reflection taking place between the antenna and the soil surface arrives at about 4.5 ns. Later in time, the backscattered signal coming from an antitank (AT) landmine appears around 6.5 ns (hyperbolic shape). Thanks to its relatively large size and metal content, as well as the strong electromagnetic contrast between this one and the sand, and to the low attenuation of the EM waves in the sand (the electric conductivity tends to zero), this landmine is easily noticeable to the naked eye. After filtering-out antenna effects (image on the right), the true time zero corresponds now to the antenna phase center, located at about 7 cm from the antenna aperture, inside the antenna, resulting in a time-shifting (note that the soil reflection and hyperbola originating from the AT landmine are shifted in time). The multiple antenna reflections have been taken away and the surface reflection appears clearer, around 1.9 ns, allowing the precise calculation of the antenna height. Moreover, the hyperbolic signature of the AT landmine is highlighted. There are some remaining oscillations which are still visible in the figure. These could be a consequence of the distinct suppositions postulated in the antenna model, mainly, (i) the condition of being in the far-field, (ii) the virtual Tx-Rx point of the antenna which is approximated at a fixed position (in reality, its position varies with frequency, the high frequencies being emitted nearer the feed point, and the low frequencies being emitted in the proportionally larger part of the antenna), and (iii) the fact that only the x -component of the electric field is supposed to be measured and that only an x -directed current source is available. These could also appear as a result of applying the inverse Fourier transform to data collected in a restricted frequency range. This chapter will show later that such oscillations are not a disadvantage for the detection and identification of AP landmines.

The surface reflection may be removed from a full GPR transect by subtracting from all measurements a mean measurement or an A-scan performed over a landmine-free area. In

order to do this, the EM properties of the subsoil should be homogenous over the transect, all measurements should be performed with the antenna situated at a constant height above the ground, and the soil surface should be totally flat. In practice, real minefields cannot satisfy these requirements. For filtering the soil surface reflection we propose to subtract from the radar signal, preliminarily filtered for antenna effects, a computed Green's function $G'(\omega)$ describing wave propagation with the antenna in air above a single interface (mine-free soil surface). The Green's function is the solution of the three-dimensional (3D) Maxwell's equations for wave propagating in multilayered media. In our case, this function accounts for wave propagation in air, including spherical divergence, and the surface reflection. To compute that Green's function, two parameters should be known: (1) the soil surface relative dielectric permittivity ϵ_r and (2) the antenna height h . These two parameters are derived using full-wave inversion of the radar signal [31] for a measurement taken in a local landmine-free area. This approach has been validated and applied with success in laboratory and field conditions for identification of the soil relative dielectric permittivity. It is worth noting that the single measurement in a local mine-free area used to estimate the soil surface dielectric permittivity can be collected at any time in any surrounding, mine-free area. Therefore, the spatiotemporal variability of the soil properties can be partly taken into account to filter the surface reflection.

Figure 16 shows data after filtering the ground surface reflection. The effect of the AT landmine is isolated, which permits to differentiate the hyperbolic signature. The response of the target is then calculated by using Eqs. (2)–(4) and can be written as:

$$R_{obj}(\omega) = G(\omega) - G'(\omega). \quad (5)$$

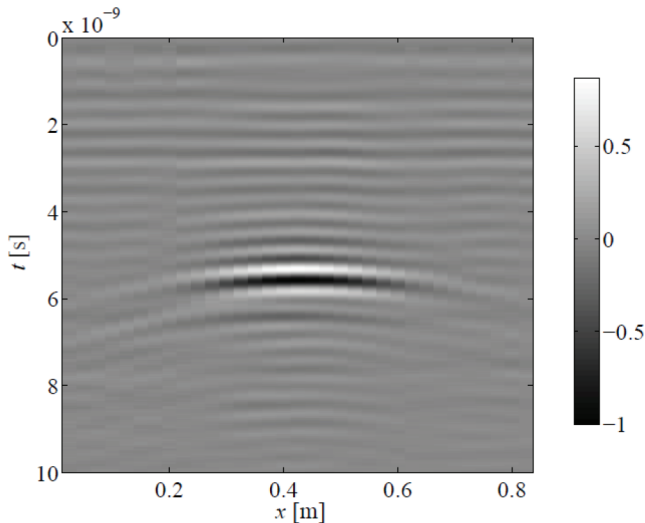


Figure 16. Results after filtering the soil surface reflection from radar data of **Figure 15** (AT landmine).

3.3. Focusing the radar image

The radar antenna transmits energy with a beamwidth pattern such that an object several centimeters away from the beam axis may be detected. As a result, objects of finite dimensions appear as hyperbolic reflectors on the B-scans. Migration techniques are used to reconstruct the reflecting structure present in the subsurface by focusing the reflections back into the true position of the object. We propose to filter out the effects of the antenna radiation pattern using the common Stolt's migration method [32], which applies a Fourier transform to back-propagate the scalar wave equation, extended in Ref. [30] for two media.

Consider the filtered signal R_{obj} as a 2D data set $R(x, z, \omega)$ with x being the distance along the scanning axis, z the depth and ω the angular frequency. Applying the Fourier transform with respect to the spatial distance x to the special frequency k_x yields an unfocused wavenumber data set

$$R(k_x, z, \omega) = \int R(x, z, \omega) e^{ik_x x} dx. \quad (6)$$

The Fourier transformation along the x coordinate makes sense only if the propagation velocity does not vary in this direction. This methodology permits variations of the propagation velocity in the z direction.

Considering the wavenumber k ($k = 2\pi/\lambda$, with λ being the wavelength in the ground) as the vector sum of k_x and k_z for one-way propagation, we have:

$$k = |\mathbf{k}| = \sqrt{k_x^2 + k_z^2} = \frac{\omega}{v} \quad (7)$$

where v is the propagation velocity in the soil.

Assuming only upward coming waves and by introducing Eq. (7) into Eq. (6), the Fourier transform of the wavefront at depth z is done by

$$R(k_x, z, \omega) = R(k_x, 0, \omega) e^{-ik_z z}. \quad (8)$$

The migrated image will be the inverse Fourier transform of Eq. (8) at $t = 0$ as

$$\hat{r}(x, z) = r(x, z, 0) = \iint R(k_x, 0, \omega) e^{-(ik_x x - k_z z)} dk_x d\omega. \quad (9)$$

Figure 17 shows results after applying Slot's migration to the data set presented in **Figures 14** and **15**.

3.4. Migration by space-time deconvolution

As described above, the aim of migration is to focus target reflections in the recorded data back into their true position and physical shape. In this respect, migration can be seen as a form of spatial deconvolution that increases spatial resolution. It is a common practice not to include in

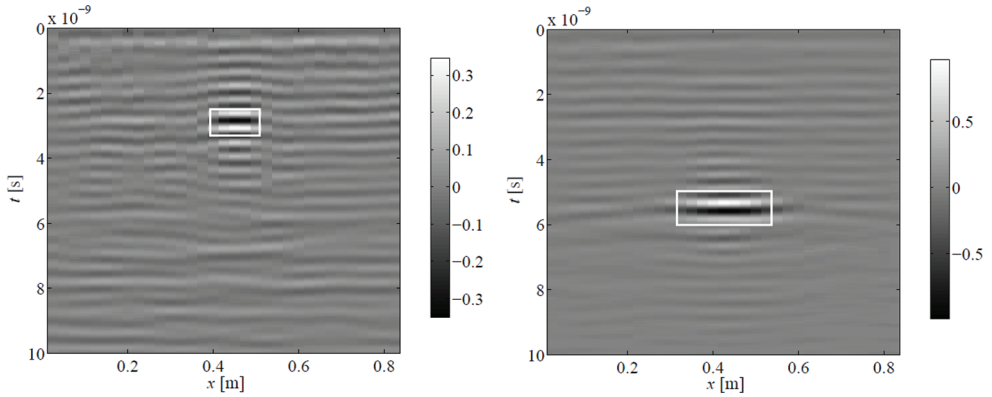


Figure 17. Results after applying the Slot's migration method for the datasets presented in **Figure 14** (PMN AP landmine, left) and **Figure 16** (AT landmine, right).

the migration approaches the characteristics of the radar system, e.g., antenna patterns, antenna impulse response, and source waveform. In this section, a migration approach that considers the system characteristics and to a certain extent, the ground characteristics, is presented [5]. Its strategy is based on the deconvolution of the collected data with the point-spread function of the radar system. As in most of migration algorithms, it is assumed that the interaction between the scatterers present in the medium is totally disregarded.

In order to perform the migration process by deconvolution, the data acquired by the UWB GPR have to be a convolution between the different layers and configurations present in the subsoil and the point-spread function of the system. This is valid under certain premises. In the interest of simplifying the analysis, a monostatic antenna configuration is taken as an example. The velocity of propagation through the propagation element can only vary in the groundward direction. The antennas are change location following a xy -plane at $z = 0$. The 3D data, $V_{rec}(x, y, z = 0, t)$ is collected following a rectangular grid with spacing Δx and Δy . Consider a point-target located in the subsoil at $\vec{r}_o = (x_o, y_o, z_o)$ in a first step, described by an IR $\Lambda_o(\vec{r}_o, t_o)$, independent of the incident direction and not necessarily a dirac impulse. For the antennas at any position $\vec{r}_a = (x_a, y_a, z = 0)$, the received voltage can be written as

$$V_{rec}(\vec{r}_a, t) = s(\vec{r}_a, \vec{r}_o, t) \otimes \Lambda_o(t) \quad (10)$$

Where $s(\vec{r}_a, \vec{r}_o, t)$ represents the voltage response of a point scatterer placed in \vec{r}_o with IR $\delta\left(t - \frac{|\vec{r}_a - \vec{r}_o|}{v}\right)$, as a function of the antenna location \vec{r}_a and time t . Additionally, for the antennas at $z = 0$ and the point scatterer at $z = z_o$, the response $s(\vec{r}_a, \vec{r}_o, t)$ is a function of \vec{r}_o and \vec{r}_a only by their difference. It is worth noting that the convolution present in Eq. (10) occurs in the time. Consider a target modeled by a group of independent point targets located in

average at the same depth $z = z_o$, the resulting voltage $V_{rec}(x_a, y_a, t)$ can be calculated as a linear combination of the voltage responses of each individual point target as:

$$V_{rec}(x_a, y_a, t) = \iint_{x,y} \int_{\tau} s(x_a - x, y_a - y, z_o, t - \tau) \Lambda_{z_o}(x, y, \tau) d\tau dx dy \quad (11)$$

Eq. (11) represents a space-time convolution along the co-ordinates x , y , and t , and can be written as

$$V_{rec}(x, y, t) = s_{z_o}(x, y, t) \otimes \Lambda_{z_o}(x, y, t) \quad (12)$$

where $\Lambda_{z_o}(x, y, t)$ is a 3D image including the feedbacks connected with the distributed targets at the positions (x, y, z_o) . The 3D matrix $s_{z_o}(x, y, t)$ symbolizes the point-spread function of the UWB GPR system for a depth $z = z_o$ and can be approximated by forward modeling for different antenna positions \vec{r}_a and a point scatterer with IR $\delta\left(t - \frac{|\vec{r}_a - \vec{r}_o|}{v}\right)$. An example of a 3D point-spread function for a UWB GPR system and a point scatterer at 6 cm of depth is given in **Figure 18**.

Even though the point-spread function $s_{z_o}(x, y, t)$ depends on the depth $z = z_o$, its contour will not be altered very much with changes in z . Basically, the point-spread function could be used for a broad depth range. Accordingly, the point-spread function $s_{z_o}(x, y, t)$ can be treated as space invariant. Therefore, the migrated image $M(x, y, t)$ can be calculated as a deconvolution of the recorded data $V_{rec}(\vec{r}_a, t)$ with the point-spread function $s_{z_o}(x, y, t)$, where z_o is chosen to be the most likely depth for an object. In the application of demining, z_o is taken 6 cm. The deconvolution can be performed in the frequency-wavenumber domain, using a Weiner filter, which makes the migration scheme very simple and not computational intensive. More details on the presented migration method can be found in Ref. [5].

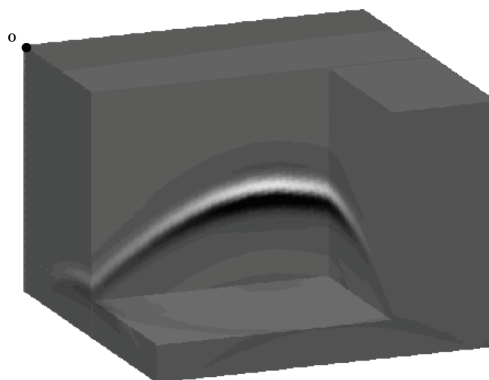


Figure 18. Synthetic C-scan of a fictive point scatterer at a depth of 6 cm below the air-ground interface, calculated by forward modeling.

Figures 19–21 show the results of the migration method on data taken by a laboratory UWB GPR described in Section 2.3, with the antennas mounted on an indoor xy -scanning table. The data are acquired over an area of $50\text{ cm} \times 50\text{ cm}$ with a step of 1 cm in both x - and y -direction. Results are shown in **Figure 19** for a PMN mine buried at 5 cm of depth in sand, in **Figure 20** for a brick of dimensions $15\text{ cm} \times 9\text{ cm} \times 6\text{ cm}$ buried at the same depth, and in **Figure 21** for a piece of 20 cm barbed wire. There is a green, three-dimensional representation of the collected data in each of the figures, which is obtained after applying first a Hilbert transformation to the A-scan in order to calculate the cover for each A-scan. As a second step, the data are plotted by an isosurface 3D plot, accentuating all the pixel of a given intensity or higher. In each figure, the raw data are plotted the left. On the right, the migrated image is displayed. For clarity, the ground reflection is suppressed in **Figures 20** and **21**. When observing the targets from above, the rounded form of the PMN mine is clearly displayed, and the form of the brick is more box-like. **Figure 21b** shows how the form of the barbed wire can be easily distinguished from the

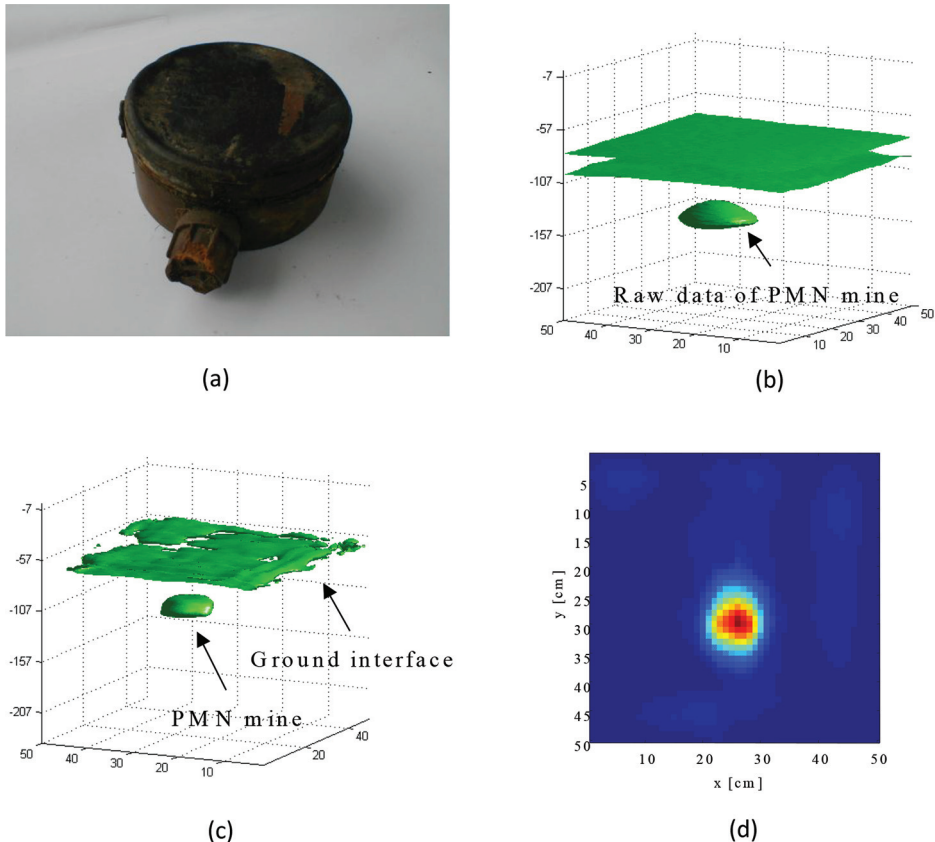
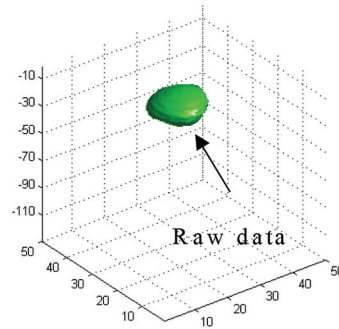


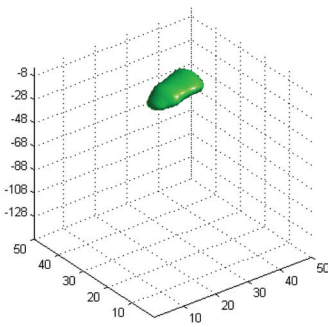
Figure 19. Results after applying deconvolution in order to focus the data collected on a PMN mine (diameter of 11 cm) located at 5 cm depth. (a) Photo of PMN mine ; (b) 3D C-scan view of raw data; (c) 3D C-scan view of migrated data; (d) 2D C-scan horizontal slide of migrated data.



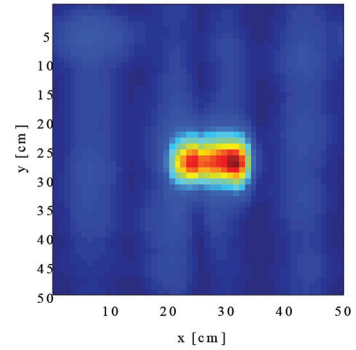
(a)



(b)



(c)



(d)

Figure 20. Results after applying deconvolution in order to focus the data collected on a brick ($15\text{cm} \times 9\text{cm} \times 6\text{cm}$) located at 5 cm depth. (a) Photo of the brick; (b) 3D C-scan view of raw data; (c) 3D C-scan view of migrated data; (d) 2D C-scan horizontal slide of migrated data.

other two forms and the three sets of pins present on the real wire are clearly noticeable. It is demonstrated with these three examples that the shape of a target in the subsoil can be extracted from the data gathered by the UWB GPR after applying the migration procedure explained above.

The aim of migration is not only to focus reflections on objects back into the true physical shape of the object but also into its true position. To illustrate the latter, an AP mine was buried under an angle of about 30° in dry sand, with the highest point of the mine at a depth of 5 cm. In the raw B-scan presented in **Figure 22a**, the strongest reflections on the mine are found in the lower right corner of the image, whereas in reality the mine (designated by the rectangular box) is situated in the middle of the image. This shift can be simply explained as follows. When

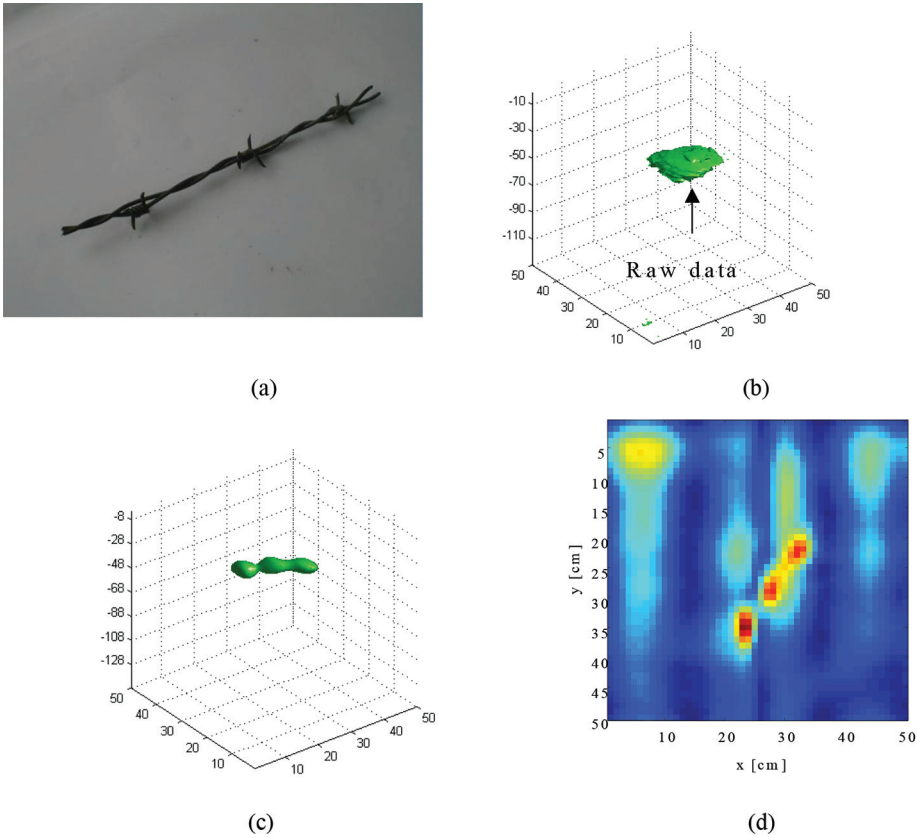


Figure 21. Results after applying deconvolution in order to focus the data collected on barbed wire (approx. 20 cm length) located at 5 cm depth. (a) Photo of the barbed wire; (b) 3D C-scan view of raw data; (c) 3D C-scan view of migrated data; (d) 2D C-scan horizontal slide of migrated data.

the antennas are right above a tilted object, the latter will appear as a strong reflection in a direction away from the receiving antenna. For the antennas in the direction perpendicular to the flat top of such a target, the reflections going toward the receiving antenna will be stronger than in the case the antennas are right above the tilted object, causing a displacement of the target in the raw data. **Figure 22b** shows how, after applying the migration using the deconvolution approach presented before, the target is found in its actual position. Results of the migration not only show that the target was at the wrong position in the raw data, but also clearly show that the target is tilted. Because of the different backscatter structures in the target, its dimensions in the z -direction could be wrongly estimated. However, the position (in time or space) of the first reflection on the target (the specular reflection) will be accurate and reliable. As a consequence, the reconstruction of the envelope of buried objects will be correct. Comparison has been done with other migration methods, like Kirchhoff migration and Stolt migration, applied on the same data, which led to less satisfactory results than the

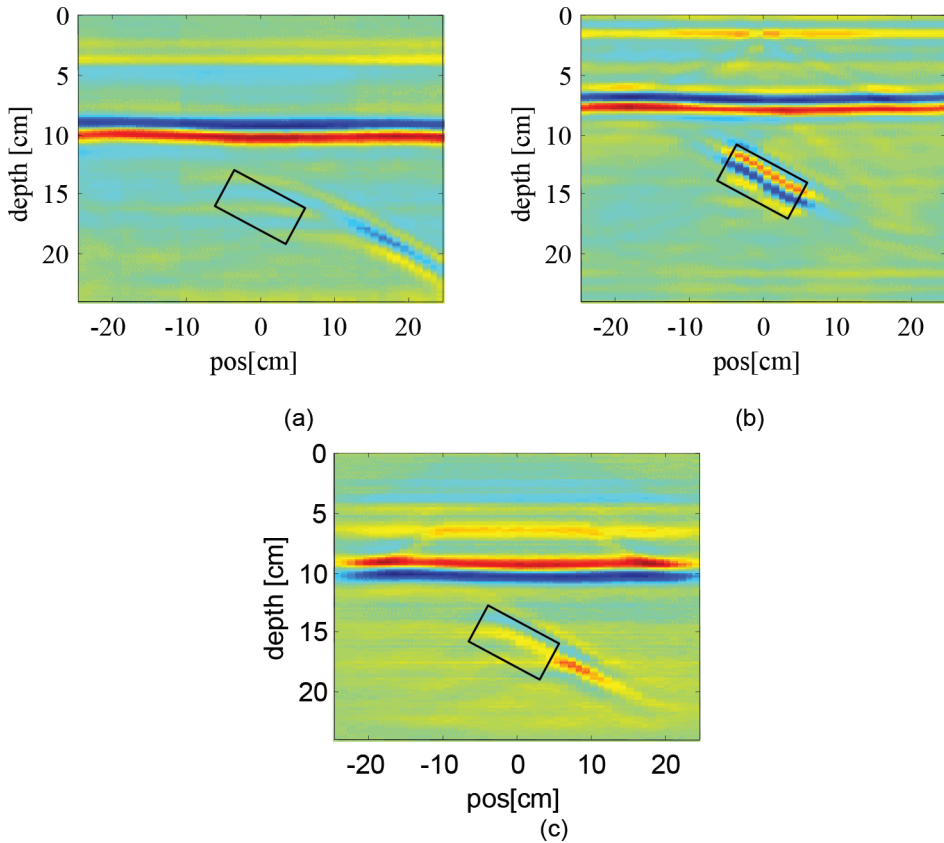


Figure 22. Oblique PMN mine under an angle of 30° . (a) Raw data, (b) image after migration by deconvolutions, and (c) image after Kirchhoff migration.

proposed deconvolution approach. In **Figure 22c**, the results after applying Kirchhoff migration can be seen. Although more information could be extracted from the migrated data, the Kirchhoff migration is not able to place the object completely back in its correct position.

3.5. Target classification

GPR may allow detecting buried objects such as metallic and nonmetallic AP landmines. However, this detection technique can be affected by false alarm rates as other reflectors (e.g., stones, metal fragments, roots) can produce similar echoes. In this regards, resonance features in backscattered signals are proposed here in order to identify unknown targets. These features can be studied in either the time-domain (TD) or the frequency-domain (FD). In Ref. [33], functions of both variables, time and frequency, are considered for this particular application. Time-frequency distributions, which are 2D functions, can reveal the time-varying frequency content of 1D signals. One of these 2D functions is the Wigner-Ville distribution (WVD), which

is widely used for target recognition. This section shows how the application of the WVD on GPR data can yield to extract important information about the physical features of AP landmines located in the subsoil.

The WVD is one of the approaches of the time-frequency representations. It has a main advantage when compared to other representations such as the short-time Fourier transform or spectrogram, which is a higher time resolution. The WVD of a 1D signal $s(t)$, $s_{WVD}(t, f)$, can be expressed as

$$s_{WVD}(t, f) = \int s_a\left(t + \frac{\tau}{2}\right) + s_a^*\left(t - \frac{\tau}{2}\right) e^{-i2\pi f\tau} d\tau, \tag{13}$$

where

$$s_a = s(t) + i\hat{s}(t) \tag{14}$$

is the analytic signal consisting of the real signal $s(t)$ and its Hilbert transform

$$\hat{s}(t) = \frac{1}{\pi} \int \frac{s(\tau)}{1 - \tau} d\tau, \tag{15}$$

and $s_a^*(t)$ is its conjugate.

Figure 23 represents the WVD of one A-scan from **Figure 16** (AT landmine). The WVD is applied only to the A-scan containing the highest amount of energy backscattered from the target, calculated after filtering and migration. The dotted line in the left figure represents raw data acquired with the SFCW UWB GPR and filtered data are presented with the solid line.

At any time (frequency) point, the WVD can be considered as the summed spectrum (correlation) of the signal power at this point and the cross-power of two signals parts, spaced symmetrically with respect to the current time point.

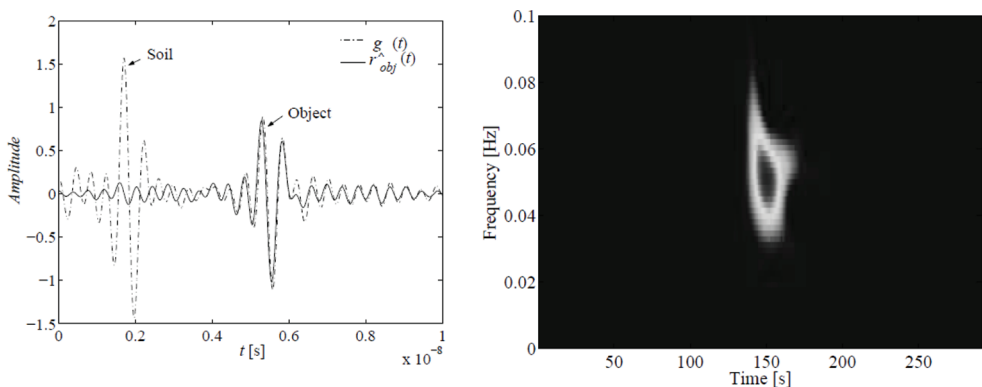


Figure 23. WVD (right) applied to a filtered and migrated A-scan data (left) for an antitank landmine buried in sand (from **Figure 16**).

As this distribution is a two-dimensional representation (matrix) of a one-dimensional signal, this transform inferred a given amount of redundancy. In order to confront this problem, Ref. [34] suggested the singular value decomposition (SVD), which is used here in conjunction with the concept of the center of mass (CM) to extract discriminant features [35].

SVD is intended for representing the WVD matrix \mathbf{W}_s with its singular values and singular vectors, which are unique for any matrix:

$$\mathbf{W}_s[m, n] = \mathbf{U}[m, m] \mathbf{\Sigma} [m, n] \mathbf{V}[n, n] \quad (16)$$

where the matrixes \mathbf{U} and \mathbf{V} consist of the left-singular and right-singular vectors, respectively, and the matrix $\mathbf{\Sigma}$ consists of the singular values. Particularly, any matrix can be disintegrated into a number of singular triplets $\{uk, \sigma_k, vk\}$, with $k = 1 \dots \min(M, N)$, where each singular value σ_k can be considered as the square root of the corresponding triplet energy. Besides, the rows and columns of \mathbf{W}_s symbolized, respectively, the distribution of the energy in time (related to the singular vectors vk) and in frequency (related to the singular vectors uk).

Since the singular values and vectors are unique for any matrix, these triplets contain energy, time, and frequency features which help in discriminating different targets. Therefore, following Ref. [35], the CM (the center of mass is the strongest point in any distribution) of the singular vectors vk and uk is used as time and frequency features and the singular value σ_k as energy feature for each triplet $\{u_k, \sigma_k, v_k\}$. After analyzing different triplets, we find that the following normalized features from the first triplet provide the best discriminant results:

$$\delta_t = \frac{1}{N} \sum_{n=1}^N n \mathbf{v}_1[n]^2 \quad (17)$$

$$\delta_f = \frac{1}{M} \sum_{m=1}^M m \mathbf{u}_1[m]^2 \quad (18)$$

$$\delta_e = \frac{\sigma_1}{\sum_{k=1}^{\min(M, n)} \sigma_k^2} \quad (19)$$

This approach is applied to different targets, including landmines, improvised explosive devices (IED), and false alarms (FA), which are buried in different types of soils. A description of the targets is done in **Table 3**.

Figure 24 shows the calculated values from Eqs. (17) to (19) for targets of **Table 3**. The features of the AP landmines are well clustered and well separated from those of the metallic false alarms and stones. The false alarms are clearly separated as well. Classification between different AP landmines (with different shapes) and between different IEDs (with different materials) could be also obtained. Results also show that the extracted features could be independent of the target depth.

Target	Type	Shape	Diameter (cm)	Metal content
C3A1	Plastic AP	Irregular	5.1	Low
PMA	Plastic AP	Rectangular	15.2	Low
Stone1	FA	Irregular	12.0	No
Metallic can	FA	Irregular	12.0	High
IED5	PVC	Cylindrical	6.3	No
IED6	PVC	Cylindrical	6.3	Low
IED7	Glass	Cylindrical	5.5	No
IED8	Glass	Cylindrical	5.5	Low
Stone2	FA	Irregular	8.0	No
Metallic debris	FA	Irregular	6.0	High

Table 3. Some characteristics of the objects used.

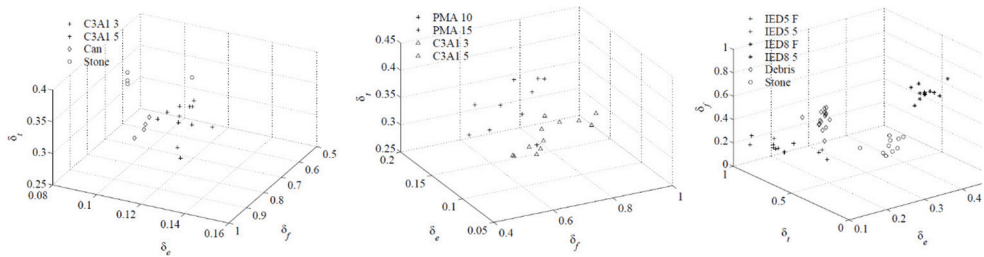


Figure 24. Extracted features from different targets buried at different depths.

4. Conclusions

In this chapter, two of the major challenges in the application of GPR in humanitarian demining operations are addressed: (i) development and testing of affordable and practical GPR-based systems, which can be used off-ground and (ii) development of robust GPR signal processing techniques for landmine detection and identification.

Different approaches developed at RMA in order to demonstrate the possibility of enhancing close-range landmine detection and identification using GPR under laboratory and outdoor conditions are summarized here. Raw GPR profiles give us a large quantity of information about the underground, and therefore performant signal processing techniques are needed to filter and improve the data quality in order to extract the right information. Data acquired using different affordable and practical GPR-based systems are used to validate a number of promising developments in signal processing techniques for target detection and identification. Removing undesirable reflections by filtering and focusing the data using migration algorithms are some of the techniques applied in image reconstruction which are introduced

here. The proposed approaches have been validated with success for the imaging, detection and classification of buried objects in laboratory and outdoor conditions. Validation has been done for different scenarios, including AP, low-metal content landmines and IEDs, and real mine-affected soils.

Acknowledgements

The work presented in this chapter was carried out at the Signal and Image Centre, École Royale Militaire, Belgium, in collaboration with the Microwave Engineering and Applied Electromagnetism Department, the Telecommunications Laboratory and the Dept. of Environmental Sciences and Land Use Planning of the UCL (Belgium), and with the Dept. de Ingeniería Eléctrica y Electrónica of the Universidad de Los Andes (Colombia). They were funded by the Ministry of Defense of Belgium in the scope of HUDEM and BEMAT projects. The Instituto Colombiano para el Desarrollo de la Ciencia y la Tecnología—Colciencias (Colombia), the Batallón Baraya (Colombia) and the Escuela de Ingenieros Militares (Colombia) are gratefully acknowledged for their outstanding support during some trials.

Author details

Olga Lucia Lopera Tellez* and Bart Scheers

*Address all correspondence to: olopera@elec.rma.ac.be

CISS Department, Royal Military Academy, Brussels, Belgium

References

- [1] MacDonald J, Looockwood J, Altshuler T, Broach T, Carin L, Harmon R, Rappaport C, Scott W, Weaver R. Alternatives for Landmine Detection. Santa Monica, CA: RAND; 2003
- [2] Acheroy M. Mine action: Status of sensor technology for close-in and remote detection of anti-personnel mines. *Near Surface Geophysics*. 2007;5:43-55
- [3] Daniels D. Ground Penetrating Radar. London: The Institution of Electrical Engineers; 2004
- [4] Lopera O. An integrated detection and classification methodology applied to ground-penetrating radar for humanitarian demining applications [PhD thesis]. Catholic University of Louvain, Royal Military Academy; 2008
- [5] Scheers B. Ultra-wideband ground-penetrating radar with application to the detection of antipersonnel landmines [PhD thesis]. Catholic University of Louvain, Royal Military Academy; 2001

- [6] Nicolaescu I, van Genderen P, van Dongen K, van Heijenoort J, Hakkaart P. Stepped frequency continuous wave radar-data preprocessing. In: Proceedings of the 2nd International Workshop on Advanced GPR; 2003; The Netherlands: Delft. pp. 177-182
- [7] Giannopoulos A. GprMax2D/3D V2.0 User Manual. Edinburgh: University of Edinburgh; 2005
- [8] Yarovoy A, Kovalenko V, Fogar A. Impact of clutter on buried object detection by ground penetrating radar. In: International Geoscience and Remote Sensing Symposium; 2003; France. pp. 755-757
- [9] Lagman A. The design of hardware and signal processing for a stepped frequency continuous wave ground penetrating radar [PhD Thesis]. Cape Town, South Africa: University of Cape Town; 2002
- [10] Sato M, Fang G, Zeng Z. Landmine detection by a broadband GPR system. In: International Geoscience and Remote Sensing Symposium; 2003; France
- [11] Chignell RJ, Hatf M. LOTUS—A real time integrated sensor suite for antipersonnel mine detection, incorporating the MINETEC GPR. In: Yarovoy, editor. Tenth International Conference on Ground Penetrating Radar; Delft, The Netherlands: TUDelft; 2004. pp. 689-692
- [12] Scheers B, Plasman Y, Piette M, Acheroy M, Vorst AV. Laboratory UWB GPR system for landmine detection. In: Proceedings of the Eighth International Conference on Ground Penetrating Radar; SPIE; 2000. pp. 747-752
- [13] Yarovoy A, Ligthart L, Schukin A, Kaploun I. Polarimetric video impulse radar for landmine detection. *Subsurface Sensing Technologies and Applications*. 2002;3:271-293
- [14] Daniels D, Curtis P, Amin R, Dittmer J. An affordable humanitarian mine detector. In: SPIE, Detection and Remediation Technologies for Mines and Minlike Targets IX; 2004. pp. 1185-1193
- [15] Sato M, Fujiwara J, Feng X, Zhou Z, Kobayashi T. Development of a hand-held GPR MD sensor system (ALIS). In: SPIE, Detection and Remediation Technologies for Mines and Minlike Targets X; 2005. pp. 1000-1007
- [16] Pajewski L, Tosti F, Kusayanagi W. Antennas for GPR systems. In: Benedetto A, editors. *Civil Engineer Applications of Ground Penetrating Radar*. Springer International Publishing; Switzerland, 2015. pp. 41-67
- [17] CEN Workshop Agreement. Humanitarian Mine Action—Test and Evaluation—Part 2: Soil Characterization for Metal Detector and Ground Penetrating Radar Performance. Available from: <http://www.mineactionstandards.org/fileadmin/MAS/documents/cen-workshop-agreements/2008>
- [18] Kanda M. *Time-Domain Measurements in Electromagnetics*. New York: Van Nostrand Reinhold Company Inc.; 1986

- [19] Klaasen JJA. An efficient method for the performance analysis of bounded-wave nuclear EMP Simulators. *Sensor and Simulation Notes*, 1992; note 345
- [20] Scheers B, Piette M, Vander Vorst A. Development of dielectric-filled TEM horn antennas for UWB GPR. In: *Millennium Conference on Antennas & Propagation AP-2000*; Davos, Switzerland, vol. II, p. 187, April 2000
- [21] Baum CE. Low-frequency-compensated TEM horn. *Sensor and Simulation Notes*. 1995; note 377
- [22] Rumsey V. *Frequency Independent Antennas*. New York, USA: Academic Press Inc; 1966
- [23] Lambot S, Slob E, van den Bosch I, Stockbroeckx B, Vanclooster M. Modeling of ground-penetrating radar for accurate characterization of the subsurface dielectric properties. *IEEE Transactions on Geoscience and Remote Sensing*. 2004;**42**:2555-2568
- [24] Michalski K, Mosig J. Multilayered media Green's functions in integral equation formulations. *IEEE Transactions on Antennas and Propagation*. 1997;**45**:508-519
- [25] Lambot S, Lopera O, Slob EC. Effect of the antenna height on the estimation of the soil electromagnetic properties using Full-Wave inverse modeling of GPR data. In: Daniels JJ, Chen CC, editors. *Proceedings of the 11th International Conference on Ground Penetrating Radar*; 2006; Columbus, Ohio, USA: The Ohio State University
- [26] Daniels D, Curtis P. MINEHOUND trials in Cambodia, Bosnia and Angola. In: Broach JT, Harmon RS, Holloway, JH Jr., editors. *Proceedings of the SPIE*; 2006; Orlando, Florida USA. Vol. 6217. DOI: 10.1117/12.663537
- [27] Sato M, Takahashi K, Fujiwara J. Development of the hand held dual sensor ALIS and its evaluation. In: *International Workshop on Advanced GPR*; 2007; Naples, Italy. IEEE; 2007
- [28] Ritter K. AN/PSS-14 mine detection system offers improved countermine capability. *Army AL&T Magazine*. 2007;**1**:54-59
- [29] Milisavljevic N. Analysis and fusion using belief functions theory of multisensor data for close-range humanitarian mine detection [PhD thesis]. Belgium: Ecole Nationale Supérieure des Telecommunications, France, Royal Military Academy; 2001
- [30] Lopera O, Slob E, Milisavljevic N, Lambot S. Filtering soil surface and antenna effects from GPR data to enhance landmine detection. *IEEE Transactions on Geoscience and Remote Sensing*. 2007;**45**(3):707-717
- [31] Lambot S, Weihermüller L, Huisman JA, Vereecken H, Vanclooster M, Slob EC. Analysis of air-launched ground-penetrating radar techniques to measure the soil surface water content. *Water Resources Research*. 2006;**42**:W11, 403. DOI: 10.1029/2006WR005,097
- [32] Ozdemir C, Demirci S, Yigit E. Practical algorithms to focus B-scan GPR images: Theory and application to real data. *Progress in Electromagnetic Research B*. 2008;**6**:109-122

- [33] Lopera O, Milisavljevic N, Daniels D, Gauthier A, Macq B. A time frequency domain feature extraction algorithm for landmine identification from GPR data. *Near Surface Geophysics*. 2008;**6**:411-421
- [34] Marinovic N, Eichmann G. An expansion of Wigner distribution and its applications. In: *Proceedings of ICASSP'85; 26-29 April 1985; Tampa, Florida USA*. IEEE. pp. 1021-1024
- [35] Savelyev T, van Kempen L, Sahli H, Sachs J, Sato M. Investigation of time-domain frequency features for GPR landmine discrimination. *IEEE Transactions on Geoscience and Remote Sensing*. 2007;**45**:118-129